Chapter 6

Pairwise velocities from cosmological N-body simulations

6.1 Introduction

Peculiar velocities contain half of the information of the phase space and are driven by gravity from the matter distribution. Therefore, at large scales, they can be used to probe the background cosmology and structure formation. Especially, the first and second moments of pairwise velocities, i.e., the mean pairwise velocity $v_{12}(r)$ and pairwise velocity dispersion $\sigma_{12}(r)$ have been widely regarded as powerful cosmological probes. Examples are given as follows.

(i) At $r \lesssim 20\ h^{-1}$Mpc, $v_{12}(r)$ can be measured from peculiar velocity surveys, and it has been used to estimate the matter density Ω_m and amplitude of density fluctuation σ_8 (e.g. Juszkiewicz et al., 2000; Feldman et al., 2003). It will become a potential dark energy probe with the coming supernova surveys (Bhattacharya et al., 2011).

(ii) At $r \lesssim 10\ h^{-1}$Mpc, $\sigma_{12}(r)$ can be obtained from galaxy redshift surveys via redshift distorted two-point correlation functions (see Appendix C for details of the two-point correlation function) or power spectra, and it has been used

to constrain Ω_m (e.g. Davis & Peebles, 1983; Jing et al., 1998, 2002; Zehavi et al., 2002; Hawkins et al., 2003) and galaxy formation models (e.g. Jing & Börner, 2004; Li et al., 2006; Tinker et al., 2007; van den Bosch et al., 2007; Li et al., 2007). Recently, Hellwing et al. (2014) show numerically that $\sigma_{12}(r)$ is a "smoking gun" for modified gravities.

(iii) At $r \lesssim 200\ h^{-1}$Mpc, galaxy clusters' $v_{12}(r)$ can be measured through the kinematic Sunyaev-Zel'dovich (kSZ) effects in microwave sky surveys, and it can be used to constrain cosmological parameters (Bhattacharya & Kosowsky, 2007), dark energy and modified gravity models (Bhattacharya & Kosowsky, 2008; Kosowsky & Bhattacharya, 2009; Mueller et al., 2014a), and neutrino mass (Mueller et al., 2014b). Especially, the mean pairwise velocity from the kSZ signal was statistically detected recently by combining the ACT microwave map and BOSS DR9 luminous galaxy catalogue (Hand et al., 2012). With the future CMB observations, the precision will be improved further and the mean pairwise velocity will become an intriguing cosmological probe.

To constrain cosmologies, we need theoretical models of $v_{12}(r)$ and $\sigma_{12}(r)$ showing how they depend on the cosmological parameters. Especially, in the precision cosmology era, the upcoming large galaxy surveys force us to work out very accurate theoretical predictions. However, pairwise velocities are not easy to model analytically (see Section 6.2 for details). The equations governing $v_{12}(r)$ and $\sigma_{12}(r)$ can be derived from the Bogoliubov-Born-Green-Kirkwood-Yvon (BBGKY) hierarchy framework (see Peebles, 1980). For example, $\sigma_{12}(r)$ is shown to depend on the three-point correlation function $\zeta(1,2,3)$, which is difficult to model (see e.g. Mo et al., 1997). There have been several attempts in this direction to theoretically model or construct fitting formulae for $v_{12}(r)$ and $\sigma_{12}(r)$; see Hamilton et al. (1991); Mo et al. (1997); Juszkiewicz et al. (1999); Sheth et al. (2001b,a).

Usually, these theoretical models/fitting formulae need to be calibrated with

cosmological N-body simulations, which are the only precise way to calculate $v_{12}(r)$ and $\sigma_{12}(r)$. However, cosmological N-body simulations have their own limitations, i.e., the N-body simulation results may be affected by the numerical methods and settings (in this thesis we call them *numerical effects*), e.g. the finite box size, force resolution (softening length), initial condition set-ups, etc.

For example, the largest scale that we can simulate is limited by the finite *box size*. Bagla & Ray (2005) and Power & Knebe (2006) have shown that a small simulated box (lack of long wavelength perturbations) tends to underestimate the correlation functions (or power spectra) at large scales. One can expect that the box size should have more severe effects on the velocity field by the following argument: in the linear theory, the continuity equation can be expressed as $\dot{\delta}_k + ikv_k = 0$ in the k-space, or equivalently $v_k \propto \delta_k/k$. Compared to the density field, the extra factor $1/k$ gives more weights to long wavelength perturbations for the velocity field. Sheth & Diaferio (2001) and Sheth et al. (2001b,a) noticed such effects on pairwise velocities and accounted for them in their analytical calculations, when comparing with the results from a simulation with a small box size. These effects were later confirmed numerically by Bagla et al. (2009). Seto (1999) and Orban (2014) used the standard perturbation theory to study box size effects on the power spectra. It will be interesting to see whether we can also understand theoretically box size effects on pairwise velocities.

Collisionless N-body codes usually adopt a *softening* force equivalent to the Plummer form, $F = Gm_1m_2\boldsymbol{r}/(r^2+\epsilon^2)^{3/2}$, to avoid close encounters (Aarseth, 1963). ϵ here is called the Plummer softening length. Generally, it is not simple to choose an optimal ϵ for an N-body simulation (see e.g. Merritt, 1996). Empirically, ϵ for a cosmological N-body simulation is set to $\sim 1/100 - 1/20$ of the mean particle distance. Smaller or larger values for ϵ can also be found in the literatures. The softening length ϵ is usually related to the smallest scale that we can trust for a simulation ("force resolution"). For example, previous studies have shown

that beyond $\sim 2\epsilon$, the effects of softening on the correlation function are small (e.g. Jenkins et al., 1998); the halo density profile and circular velocity profile are convergent at scales beyond ϵ for simulations with different softening lengths (e.g. Navarro et al., 1996). However, the softening effects on pairwise velocities can be larger, as shown by Suto & Jing (1997). Based on the cosmic virial theorem (Peebles, 1980), they performed a detailed analysis of the softening effects on $\sigma_{12}(r)$ at small scales ($r < 3\ h^{-1}$Mpc), and shown that the softening force can reduce $\sigma_{12}(r)$ at scales much larger than ϵ. In this chapter, we use N-body simulations and theoretical calculations to show that the softening force actually has effects on $\sigma_{12}(r)$ at *all* scales (even at scales as large as $\sim 100\ h^{-1}$Mpc). This result is surprising in the first impression given that we usually expect the softening force to affect simulation results at small scales only. We provide methods to correct the softening effects on $\sigma_{12}(r)$ at large scales.

Since pairwise velocities will become powerful probes in the coming decades, and theoretical models of $v_{12}(r)$ and $\sigma_{12}(r)$ have to be calibrated with simulations, understanding all these numerical effects quantitatively will be very important. In this chapter, we report a detailed investigation on the box size and softening effects, and we provide correction methods to correct them. We also test the effects from the methods of generating initial conditions (e.g. grid or glass, Zel'dovich approximation or 2nd-order Lagrangian Perturbation Theory).

This chapter is organized as follows. We outline the definitions and theoretical basis in Section 6.2, and summarise our simulation methodology and details in Section 6.3. The effects from the finite box size, softening length and initial conditions are presented and discussed in Section 6.4, 6.5 and 6.6 respectively. We summarise our results and give conclusions in Section 6.7.

6.2 Theoretical basis

6.2.1 Mean pairwise velocity

The mean pairwise velocity along the line-of-separation is defined as

$$v_{12}(r) \equiv \langle [\boldsymbol{v}_1(\boldsymbol{r}') - \boldsymbol{v}_2(\boldsymbol{r}' + \boldsymbol{r})] \cdot \hat{\boldsymbol{r}} \rangle \,, \tag{6.1}$$

where $\boldsymbol{v}_i(\boldsymbol{r}')$ is the peculiar velocity of particle i at position $\boldsymbol{r}'$, and $\langle \cdots \rangle$ means the average over all pairs which have a separation of r. The mean pairwise velocity only depends on the magnitude of $\boldsymbol{r}$ due to the assumption of isotropy. According to the conservation of pairs, which can be derived from the BBGKY hierarchy equations (Peebles, 1980, §71), the mean pairwise velocity is related to the two-point correlation function $\xi(r)$ as

$$-\frac{v_{12}(r)}{Hr} = \frac{a}{3[1+\xi(r)]} \frac{\partial \bar{\xi}(x,a)}{\partial a}, \tag{6.2}$$

where x is the comoving distance $x = r/a$, H is the Hubble parameter, and the averaged correlation function $\bar{\xi}(x,a)$ is defined as

$$\begin{aligned} \bar{\xi}(x,a) &\equiv \frac{3}{x^3} \int_0^x dy \xi(y,a) y^2 \\ &= \frac{1}{2\pi^2} \int_0^\infty dk k^2 P(k,a) W(kx). \end{aligned} \tag{6.3}$$

Here, $P(k,a)$ is the matter power spectrum, and $W(y) = 3(\sin y - y \cos y)/y^3$.

At small scales ($r \lesssim 0.1\ h^{-1}$Mpc), the clustering is stable (i.e., the physical relative velocity is zero), and thus the mean pairwise velocity measuring the peculiar relative velocity should be cancelled out by the Hubble expansion velocity, i.e., $v_{12}(r) = -Hr$. At large scales ($r \gtrsim 20\ h^{-1}$Mpc), the linear approximation works well (see e.g. Juszkiewicz et al., 1999; Sheth et al., 2001b), i.e., $v_{12}(r) = -2Hrf\bar{\xi}/3(1+\xi)$, where $f \equiv \partial \ln D / \partial \ln a$ is the linear growth rate, and $D(a)$ is the linear growth factor which measures how fast the density perturbations grow linearly. This linear treatment is frequently adopted to predict $v_{12}(r)$ at large scales; see e.g. Bhattacharya & Kosowsky (2007), Kosowsky

& Bhattacharya (2009) and Mueller et al. (2014a). At extremely large scales, $v_{12}(r \to \infty) = 0$ since particles become uncorrelated.

Theoretical models of $v_{12}(r)$ can be found in Hamilton et al. (1991), Mo et al. (1997), Juszkiewicz et al. (1999), and Sheth et al. (2001b,a).

6.2.2 Pairwise velocity dispersion

The pairwise velocity dispersion in the line-of-separation direction is defined as

$$\sigma_{12}(r) = \left\langle \{[\boldsymbol{v}_1(\boldsymbol{r}') - \boldsymbol{v}_2(\boldsymbol{r}' + \boldsymbol{r})] \cdot \hat{\boldsymbol{r}}\}^2 \right\rangle^{1/2}. \tag{6.4}$$

The equation governing the pairwise velocity dispersion is (Peebles, 1980, §72)

$$\begin{aligned} \frac{\partial}{\partial t}[1+\xi(x)]v^\alpha &+ \frac{\dot{a}}{a}[1+\xi(x)]v^\alpha \\ &+ \frac{1}{a}\frac{\partial}{\partial x^\beta}(1+\xi)\left\langle v_{12}^\alpha v_{12}^\beta \right\rangle \\ &+ \frac{2Gm}{a^2}\frac{x^\alpha}{x}(1+\xi) + 2G\rho_b a \frac{x^\alpha}{x^3}\int_0^x d^3x\xi(x) \\ &+ 2G\rho_b a \int d^3x_3 \zeta(1,2,3)\frac{x_{31}^\alpha}{x_{31}^3} = 0, \end{aligned} \tag{6.5}$$

where $v^\alpha = \langle v_2^\alpha - v_1^\alpha \rangle$ is the $\alpha-$component of the mean relative peculiar velocity, x_{ij}^α is the $\alpha-$component of the distance vector between particle i and j, $\boldsymbol{x}_{ij} = \boldsymbol{x}_j - \boldsymbol{x}_i$, m is the particle mass, ρ_b is the background matter density, and the pairwise velocity dispersion is related to the term $\left\langle v_{12}^\alpha v_{12}^\beta \right\rangle$.

At small scales, $\sigma_{12}(r)$ can be calculated from the cosmic virial theorem (Peebles, 1980, §75). At large scales, particles tend to be independent from each other, and thus $\sigma_{12}^2(r \to \infty) = 2\langle v_1^2 \rangle /3$, where $\langle v_1^2 \rangle$ is the variance of peculiar velocities and can be determined from the cosmic energy equation (Peebles, 1980, §74), and the factor of 2 comes from pairing of particles while the factor of 1/3 originates from the fact that we only consider the line-of-separation direction. Due to its dependence on the three-point correlation function, it's very difficult to model $\sigma_{12}(r)$ through Equation (6.5); see Mo et al. (1997) and Sheth et al.

(2001b). Some attempts to model $\sigma_{12}(r)$ can be found in Mo et al. (1997); Sheth et al. (2001b,a).

6.2.3 Cosmic virial theorem

At small scales, the clustering is stable and in "statistical equilibrium", Equation (6.5) can be approximated to the cosmic virial theorem (CVT; see Peebles, 1980, §75)

$$\sigma_{12}^2(r) = \frac{6G\rho_b}{\xi(r)} \int_r^\infty \frac{dr'}{r'} \int d\boldsymbol{z} \frac{\boldsymbol{r}' \cdot \boldsymbol{z}}{z^3} \zeta(r', z, |\boldsymbol{r}' - \boldsymbol{z}|), \tag{6.6}$$

where the three-point correlation function can be approximated as

$$\zeta(a, b, c) = Q \left[\xi(a)\xi(b) + \xi(b)\xi(c) + \xi(c)\xi(a)\right]. \tag{6.7}$$

Q here is assumed to be a constant.

CVT relates the mean square of pairs' relative velocities ("kinetic energy") to pairs' potential energies, which are dominated by the interactions between the pairs and other particles reflected by the three-point correlation function in Equation (6.6).

The softening force modifies CVT in two aspects (Suto & Jing , 1997): (i) it changes the Newtonian gravity into the Plummer form; (ii) it suppresses the two-point correlation function $\xi(r)$ at small scales and turns it into $\xi(r;\epsilon)$ (see Section 6.5).

Therefore, with the softening force, CVT becomes

$$\sigma_{12}^2(r;\epsilon) = \frac{6G\rho_b}{\xi(r;\epsilon)} \int_r^\infty \frac{dr'}{r'} \int d\boldsymbol{z} \frac{\boldsymbol{r}' \cdot \boldsymbol{z}}{(z^2+\epsilon^2)^{3/2}} \zeta(r', z, |\boldsymbol{r}' - \boldsymbol{z}|; \epsilon), \tag{6.8}$$

where $\zeta(a, b, c; \epsilon) = Q \left[\xi(a;\epsilon)\xi(b;\epsilon) + \xi(b;\epsilon)\xi(c;\epsilon) + \xi(c;\epsilon)\xi(a;\epsilon)\right]$.

6.2.4 Cosmic energy equation

At large scales, $\sigma_{12}^2(r)$ approaches $2\left\langle v_1^2\right\rangle/3$, where $\left\langle v_1^2\right\rangle$ can be determined from the cosmic energy equation (CEE; see Peebles, 1980, §74),

$$\left\langle v_1^2\right\rangle = \frac{3}{2}\Omega_m(a)H^2(a)a^2 I_2(a)\left[1-\frac{1}{aI_2(a)}\int_0^a daI_2(a)\right], \tag{6.9}$$

where

$$I_2(a) = \int_0^\infty dx x\xi(x,a). \tag{6.10}$$

CEE is the Newtonian energy conservation equation expressed in the expanding universe, and relates the mean square of particles' peculiar velocities ("kinetic energy") to particles' potential energies, which are mainly due to the interactions between particles reflected by the two-point correlation function.

Similar to CVT, with the softening force, CEE is modified into

$$\left\langle v_1^2\right\rangle_\epsilon = \frac{3}{2}\Omega_m(a)H^2(a)a^2 I_2(a;\epsilon)\left[1-\frac{1}{aI_2(a;\epsilon)}\int_0^a daI_2(a;\epsilon)\right], \tag{6.11}$$

where

$$I_2(a;\epsilon) = \int_0^\infty dx\frac{x^2\xi(x,a;\epsilon)}{\left(x^2+\epsilon^2\right)^{1/2}}. \tag{6.12}$$

6.2.5 Standard perturbation theory

In the standard perturbation theory (SPT; see Bernardeau et al., 2002, for a review) which takes mode-couplings into account, the one-loop non-linear matter power spectrum is (Suto & Sasaki, 1991; Makino et al., 1992)

$$P_{\rm SPT}(k) = P_{\rm lin}(k) + P_{22}(k) + P_{13}(k), \tag{6.13}$$

where

$$\begin{aligned} P_{22}(k) &= \frac{1}{98}\frac{k^3}{4\pi^2}\int_0^\infty drP_{\rm lin}(kr)\times \\ &\quad \int_1^{-1} dxP_{\rm lin}\left(k\sqrt{1+r^2-2rx}\right)\frac{(3r+7x-10rx^2)^2}{(1+r^2-2rx)^2}, \end{aligned} \tag{6.14}$$

$$P_{13}(k) = \frac{1}{252}\frac{k^3}{4\pi^2}P_{\rm lin}(k)\int_0^\infty dr P_{\rm lin}(kr)\left[\frac{12}{r^2} - 158 + 100r^2 - 42r^4 + \frac{3}{r^2}(r^2-1)^3(7r^2+2)\ln\left|\frac{1+r}{1-r}\right|\right], \quad (6.15)$$

and $P_{\rm lin}(k)$ is the linear power spectrum.

Seto (1999) and Orban (2014) have shown that the one-loop SPT is helpful for understanding box size effects on the power spectrum. In this chapter, we will use the one-loop SPT to discuss box size effects on pairwise velocities.

6.3 Numerical simulations

We use 512^3 particles as a Monte Carlo sample of the dark matter phase space distribution $f(\boldsymbol{r}, \boldsymbol{p}, t)$ in the ΛCDM model. The initial conditions are generated using the 2LPTic code[1]. We evolve the simulations with the TreePM Gadget-2 code (Springel, 2005). The cosmological parameters used in our simulations are $\Omega_m = 0.3, \Omega_b = 0.04, \Omega_\Lambda = 0.7, h = 0.7, \sigma_8 = 0.9$, and $n_s = 0.96$.

To test the effects from initial conditions (ICs), we use both the grid and glass (Baugh et al., 1995; White, 1996) schemes to generate uniform particle distributions, and then perturb their positions and velocities both with the Zel'dovich approximation (ZA; Zel'dovich, 1970) and 2nd-order Lagrangian perturbation theory (2LPT; Crocce et al., 2006).

To study the effects from softening lengths, we perform simulations ($L_{\rm box} = 500\ h^{-1}$Mpc) with comoving softening lengths $\epsilon = 10, 30, 90$ and $270\ h^{-1}$kpc, which correspond to $\sim 1/100, \sim 1/30, \sim 1/10$ and $\sim 1/4$ of the mean particle distance respectively. Note that the Gadget code uses spline softening scheme (Springel et al. , 2001), and ϵ mentioned above are the equivalent Plummer softening lengths.

To examine box size effects, we follow the method in Bagla & Ray (2005)

[1] http://cosmo.nyu.edu/roman/2LPT

and Power & Knebe (2006), where we use the same simulation box size $L_{\rm box}$ for all numerical experiments. To mimic a smaller box, we chop off the initial perturbations with $k < fk_{\rm box}$, where $k_{\rm box} = 2\pi/L_{\rm box}$, and thus we create a simulation with an effective box size $L_{\rm eff} = fL_{\rm box}$. Especially, perturbations with the same wave number k in simulations with different $L_{\rm eff}$ have the same phases. In this setting, the only difference among different simulations is the lack of long wavelength perturbations, and the cosmic variance and small statistics of particle pairs problems are thus avoided. We perform two sets of simulations: (i) $L_{\rm box} = 500\ h^{-1}$Mpc, $f = 1.0, 0.5, 0.25, 0.125$ and (ii) $L_{\rm box} = 1000\ h^{-1}$Mpc, $f = 1.0, 0.5, 0.25, 0.125$. They show similar results, and if not specified, we mainly present the results of the former in this chapter.

The details of our simulations are summarised in Table 6.1.

6.4 Box size effects

6.4.1 Power spectra

The power spectra from simulations with different $L_{\rm eff}$ are shown in the upper row of Figure 6.1. Simulations with smaller box sizes tend to underestimate the power spectra at scales close to $k_{\rm eff} = 2\pi/L_{\rm eff}$. This is clearer for simulations with $L_{\rm eff} \lesssim 100\ h^{-1}$Mpc. Our results confirm those of Power & Knebe (2006).

The underestimation mainly comes from the lack of mode-couplings between $k \geq k_{\rm eff}$ and $k < k_{\rm eff}$, which can be confirmed qualitatively from the one-loop SPT calculations (the middle row of Figure 6.1); also see Seto (1999) and Orban (2014). Interestingly, the SPT calculations can also explain the non-zero power spectra at $k_{\rm box} \leq k \leq k_{\rm eff}$ observed in the simulations. The powers at such scales k originate from the couplings between modes k_1 and k_2, which satisfy that $k_1 \geq k_{\rm eff}$, $k_2 \geq k_{\rm eff}$ and $\boldsymbol{k} = \boldsymbol{k}_1 + \boldsymbol{k}_2$.

The ratio between the power spectrum of a chopped model and that of the

Table 6.1: Details of cosmological N-body simulations

Name	ZA or 2LPT	Grid or glass	$z_{\rm in}$	$L_{\rm box}$ (h^{-1}Mpc)	$L_{\rm eff}$ (h^{-1}Mpc)	Softening Length ϵ (h^{-1}kpc)
FIDUCIAL	2LPT	Grid	100	500	500	10
ZA	ZA	Grid	100	500	500	10
GLASS	2LPT	Glass	100	500	500	10
500-f0.5	2LPT	Grid	100	500	250	10
500-f0.25	2LPT	Grid	100	500	125	10
500-f0.125	2LPT	Grid	100	500	62.5	10
1000-f1.0	2LPT	Grid	100	1000	1000	20
1000-f0.5	2LPT	Grid	100	1000	500	20
1000-f0.25	2LPT	Grid	100	1000	250	20
1000-f0.125	2LPT	Grid	100	1000	125	20
SL-30	2LPT	Grid	100	500	500	30
SL-90	2LPT	Grid	100	500	500	90
SL-270	2LPT	Grid	100	500	500	270

Table 6.2: Best-fitted parameters for $R_i(k)$ in simulations and SPT calculations.

i	$L_{\rm eff}$ (h^{-1}Mpc)	α	β	γ
sim	62.5	0.78	0.68	0.72
	125	0.22	0.59	0.64
	250	0.040	0.54	0.55
SPT	62.5	0.80	0.097	-9.7×10^{-4}
	125	0.21	0.084	0.034
	250	0.033	0.083	0.056

fiducial model at $k \geq k_{\rm eff}$ can be approximately fitted as

$$R_i(k) = \frac{P_{i,L}(k)}{P_{i,L=\infty}(k)} = 1 + \alpha \left[\left(\frac{\beta}{k+\gamma} \right)^3 - \frac{\beta}{k+\gamma} \right], \tag{6.16}$$

where α, β and γ are free parameters, and $i = \{\text{sim, SPT}\}$. The best-fitted $R_i(k)$ for different simulations/SPT calculations with different $L_{\rm eff}$ are shown as thick dashed lines in Figure 6.1, and summarised in Table 6.2. Here we only intend to capture the general features of $R_i(k)$, which will be used to understand the box size effects on pairwise velocities in later discussions.

Noticing the applicability of the SPT to explain box size effects qualitatively, we will see to what degree the SPT can correct these effects. The results are shown in the lower row of Figure 6.1. In the "SPT corrections (SC)", we approximate the corrected power spectrum as

$$P_{\rm SC}(k) = P_{{\rm sim},L}(k) \times \frac{P_{{\rm SPT},L=\infty}(k)}{P_{{\rm SPT},L}(k)}. \tag{6.17}$$

The SPT corrections can notably improve the simulated power spectrum with a small box size, especially for scales close to $k_{\rm eff}$. However, for $k < k_{\rm eff}$, the SPT corrections tend to overestimate $P(k)$.

An improved correction method at these scales is to replace the numerical power spectrum with the linear one directly, given that if $k_{\rm eff}$ is in the linear or

quasi-linear regime, i.e.,

$$P_{\rm LSC}(k) = \begin{cases} P_{\rm lin}(k), k \leq k_{\rm eff} \\ P_{{\rm sim},L}(k) \times \frac{P_{{\rm SPT},L=\infty}(k)}{P_{{\rm SPT},L}(k)}, k \geq k_{\rm eff}. \end{cases} \quad (6.18)$$

In this chapter, we use the Eisenstein-Hu (EH, Eisenstein & Hu, 1998) power spectrum as the linear power spectrum, $P_{\rm lin}(k)$.

Equation (6.18) is called the "linear+SPT corrections (LSC)" hereafter, and will be used to correct box size effects on the correlation functions and pairwise velocities. Interested readers can refer to Tormen & Bertschinger (1996) and Cole (1997) for another correction method, the Mode Adding Procedure (MAP), which uses the Zel'dovich approximation and temporal perturbations to add the perturbations with wavelength larger than the simulated box size.

6.4.2 Correlation functions

Similar to the case of $P(k)$, simulations with smaller box sizes underestimate the correlation functions at large scales (the upper row of Figure 6.2), which are consistent with the results in Bagla & Ray (2005) and Power & Knebe (2006). At scales comparable to $L_{\rm eff}$, the underestimation can even be larger than 50%.

Bagla & Prasad (2006) suggests that box size effects on the correlation functions can be corrected by adding the linear perturbations with $k < k_{\rm eff}$ [the "linear corrections (LC)"], i.e.,

$$\xi_{\rm LC}(r) = \xi_{\rm sim}(r) + \Delta\xi_{\rm lin}(r), \quad (6.19)$$

where

$$\Delta\xi_{\rm lin}(r) = \frac{1}{2\pi^2 r} \int_0^{k_{\rm eff}} dk P_{\rm lin}(k) \sin(kr) k. \quad (6.20)$$

In the middle row of Figure 6.2, we confirm that the linear corrections can significantly improve the simulated results, especially for scales comparable to $L_{\rm eff}$. However, if the simulation has a very small box size (e.g. $L_{\rm eff} = 62.5\ h^{-1}$Mpc),

the linear corrections are not good enough; for example, at $r \sim 1\ h^{-1}$Mpc, the underestimation is over 30%. The failure is mainly due to the ignorance of mode-couplings in the linear theory. An improvement is to use the linear+SPT corrections, i.e.,

$$\begin{aligned} \xi_{\rm LSC}(r) &= \frac{1}{2\pi^2 r}\int_0^\infty dk P_{\rm LSC}(k)\sin(kr)k \\ &= \xi_{\rm sim}(r) + \Delta\xi_{\rm lin}(r) + \Delta\xi_{\rm SPT}(r), \end{aligned} \tag{6.21}$$

where

$$\Delta\xi_{\rm SPT}(r) = \frac{1}{2\pi^2 r}\int_{k_{\rm eff}}^{\sim k_{\rm Ny}} dk P_{\rm sim}(k)\left[\frac{P_{{\rm SPT},L=\infty}(k)}{P_{{\rm SPT},L}(k)} - 1\right]\sin(kr)k. \tag{6.22}$$

Empirically, a value comparable to the Nyquist wavenumber, $k_{\rm Ny}$, for the upper limit of the integral in Equation (6.22) gives convergent results, since box size effects at such small scales are tiny. In this chapter, we adopt the value of $2k_{\rm Ny}$ for calculations. The linear+SPT corrected results are shown in the lower row of Figure 6.2. The linear+SPT correction method can further improve the linear corrected results, especially in the quasi-linear regime ($\sim 1 - 10h^{-1}$Mpc).

6.4.3 Mean pairwise velocities

As shown in the upper row of Figure 6.3, simulations with small $L_{\rm eff}$ lead to underestimations of scale and magnitude of the minimum value for $v_{12}(r)$. At small scales ($r \ll L_{\rm eff}$), $v_{12}(r)$ is not affected by the lack of long wavelength perturbations, but at large scales ($r \sim L_{\rm eff}$), its magnitude is significantly suppressed.

To understand the origins of these effects, we calculate the mean pairwise velocities from (i) the linear power spectrum, (ii) the halofit nonlinear power spectrum (Smith et al., 2003; Takahashi et al., 2012), and (iii) the halofit power spectrum modulated by the ratio $R_i(k)$ fitted from simulations/SPT calculations. All of them are chopped off at $k < k_{\rm eff}$ to mimic box size effects. For the halofit power spectrum, we adopt the 2012 version given by Takahashi et al. (2012). The results are summarised in Figure 6.4.

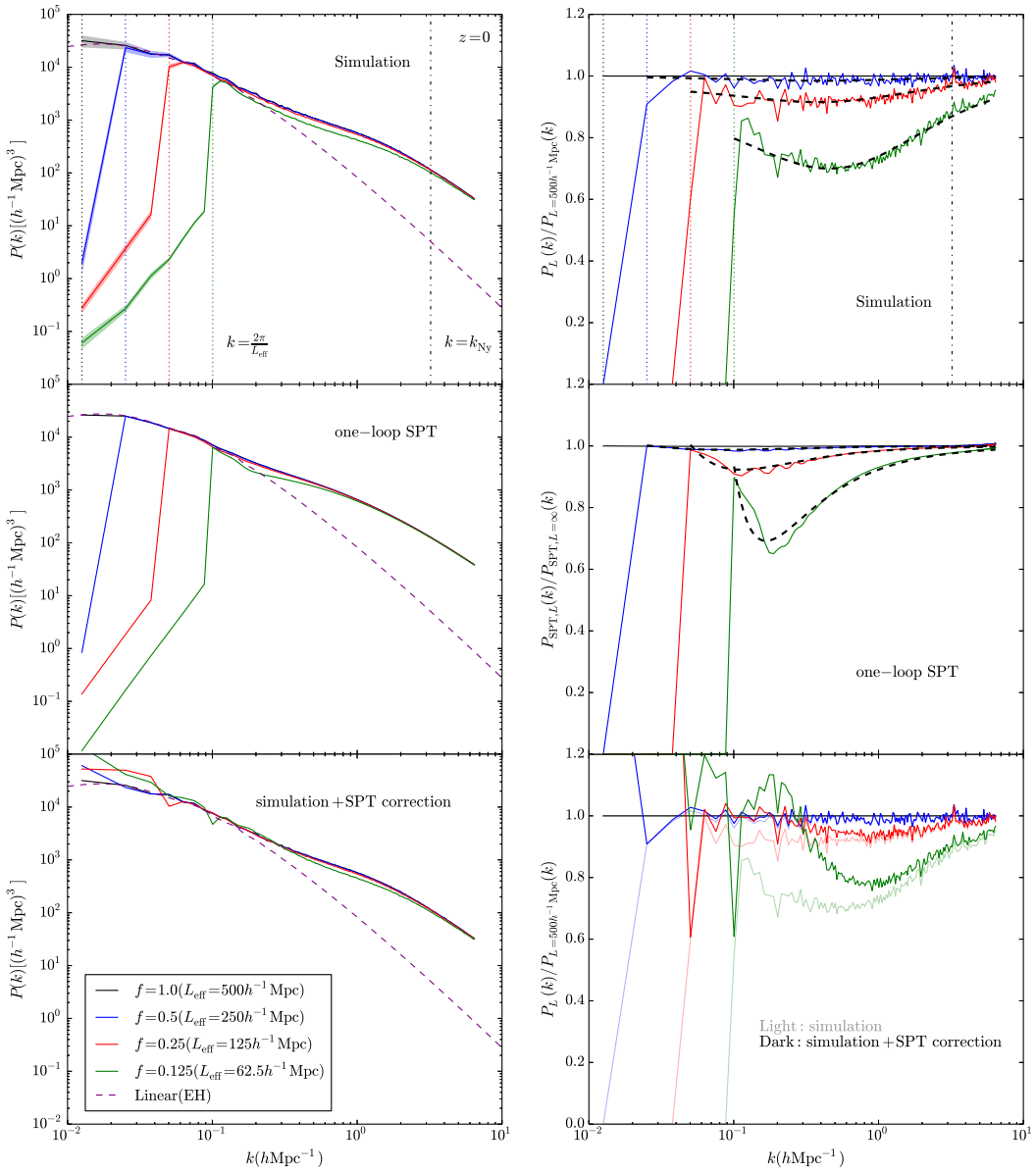

Figure 6.1: Box size effects on the power spectra. The upper, middle and lower rows present the results from simulations, one-loop SPT calculations and simulated power spectra with SPT corrections respectively. The left (right) column gives the power spectra (the ratios with respect to the fiducial simulation). The Eisenstein-Hu (EH) linear power spectra are shown with purple dashed lines in the left column. The dotted lines in the upper row mark the effective wave numbers $k_{\rm eff} = 2\pi/L_{\rm eff}$ for different simulations, and the dash-dotted lines mark the Nyquist wave numbers. The thick black dashed lines show the best-fits of $R(k)$ [Equation (6.16)] for simulations and SPT calculations.

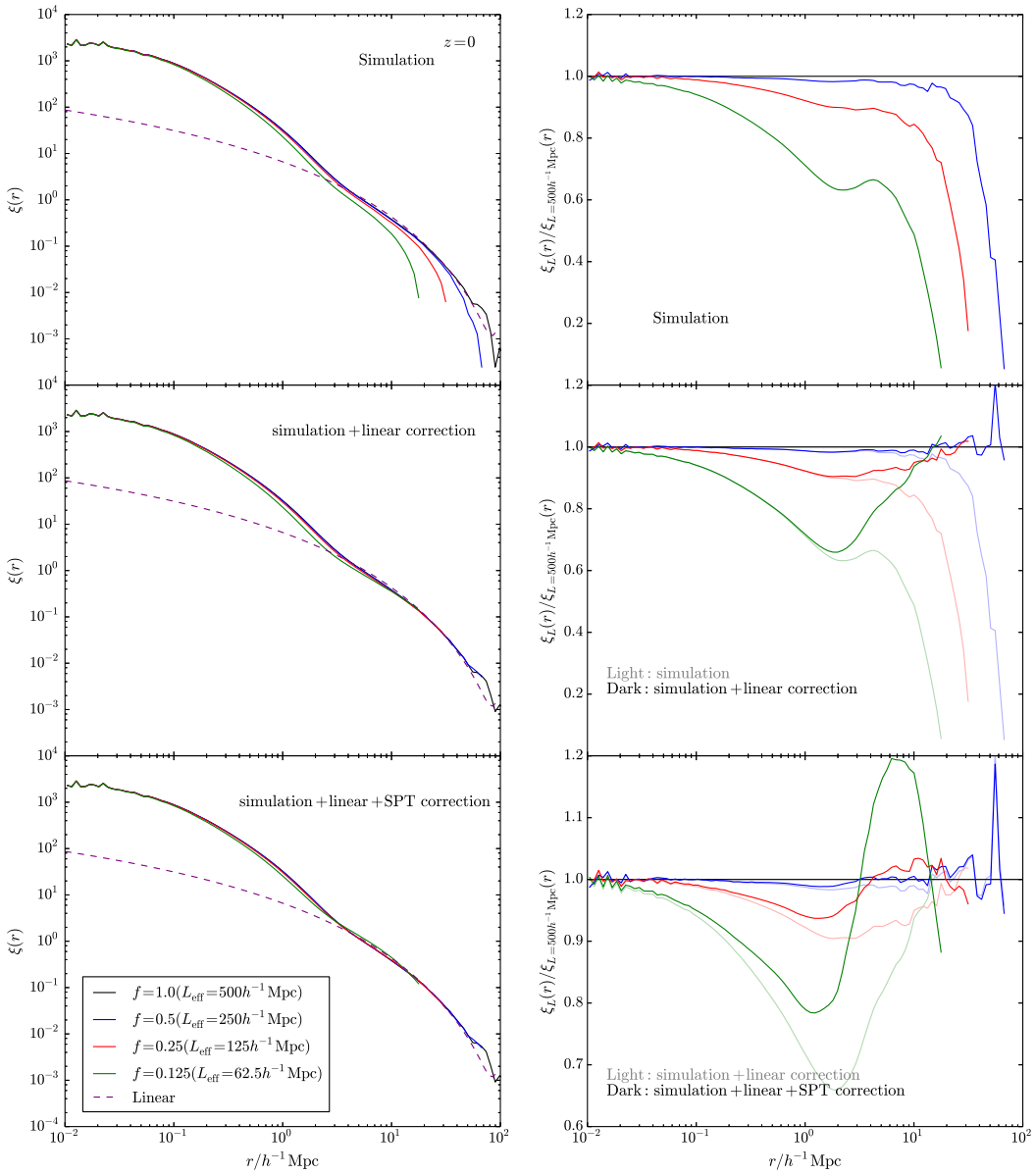

Figure 6.2: Box size effects on the correlation functions. Similar to Figure 6.1, the upper, middle and lower rows present the results from simulations, simulated correlation functions after linear corrections and simulation+linear+SPT corrections respectively. The left (right) column gives the correlation functions (the ratios with respect to the fiducial simulation). The linear correlation functions shown with dashed lines in the left column are calculated from the EH power spectrum. To give direct comparisons between the simulated and different corrected results, simulated (linear corrected) results are shown with light colors in the middle (lower) right panel.

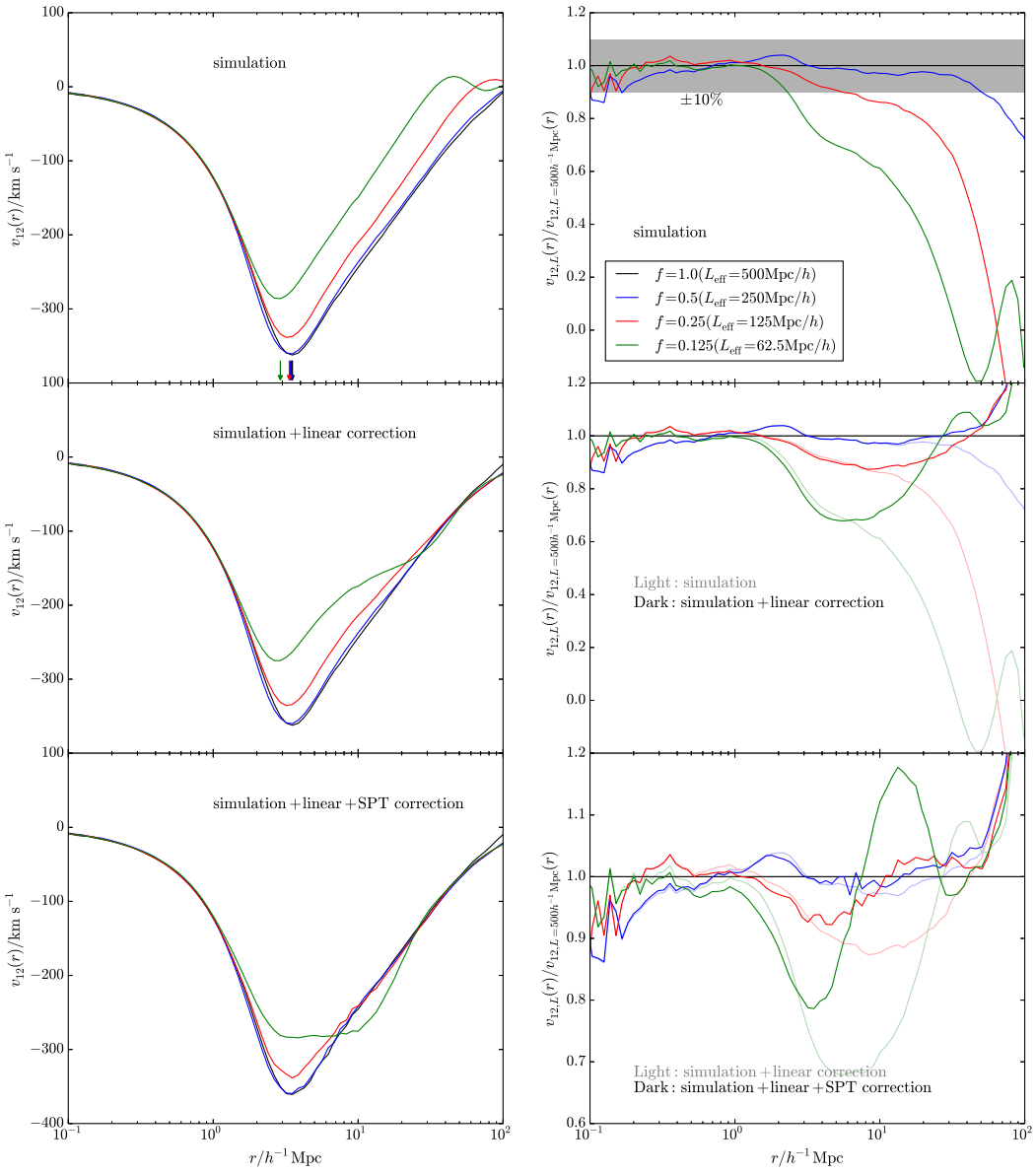

Figure 6.3: Box size effects on the mean pairwise velocities. Similar to Figure 6.2, the upper, middle and lower rows present the results from simulations, simulated $v_{12}(r)$ after linear corrections and simulation+linear+SPT corrections respectively. The left (right) column gives the mean pairwise velocities (the ratios with respect to the fiducial simulation). The arrows in the upper left panel mark the scales of minimum $v_{12}(r)$ for simulations with different $L_{\rm eff}$. The shaded region in the upper right panel represents the ±10% precision level.

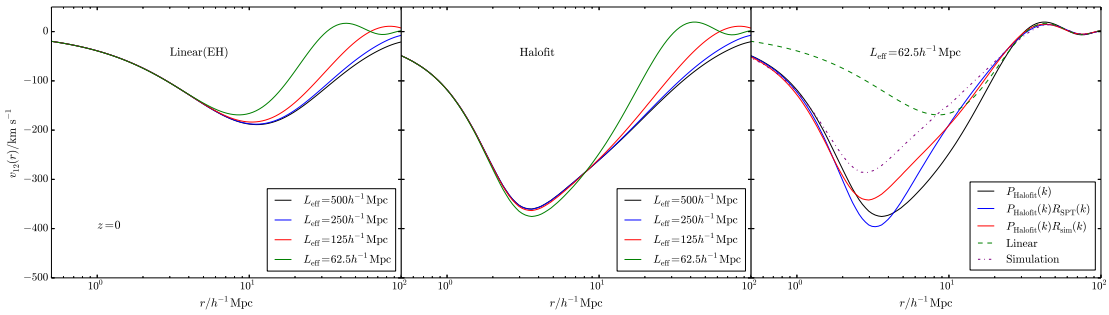

Figure 6.4: Mean pairwise velocities calculated from different power spectra. The left (middle) panel shows the results from the linear (halofit) power spectra chopped off at $k < k_{\rm eff}$. The right panel compares $v_{12}(r)$ calculated from different power spectra and from the simulation ($L_{\rm eff} = 62.5h^{-1}$Mpc).

The linear calculation results (left panel of Figure 6.4) have similar behaviours as the simulated ones, especially the suppressions at large scales ($r \sim L_{\rm eff}$). Although the linear theory predicts similar underestimations on the valley scale and magnitude as the simulations, it fails to account for them quantitatively, i.e., the valley scales (magnitudes) are overestimated (underestimated). Actually, the valley of the simulated $v_{12}(r)$ comes from nonlinear clusterings (see Sheth et al., 2001b), and cannot be explained by the linear theory.

Interestingly, the halofit model, which contains non-linear information, successfully predicts the scales and magnitudes of minimum $v_{12}(r)$ for simulations with large $L_{\rm eff}$, but not for small $L_{\rm eff}$ (middle panel of Figure 6.4). This suggests that the underestimations of the scales and magnitudes of minimum $v_{12}(r)$ in the simulations should originate from the lack of mode-couplings between $k < k_{\rm eff}$ and $k \geq k_{\rm eff}$. This is confirmed by looking at the calculated $v_{12}(r)$ from the halofit power spectrum modulated by $R_i(k)$ (right panel of Figure 6.4).

In the example of $L_{\rm eff} = 62.5\ h^{-1}$Mpc, the model of $P_{\rm halofit}(k)R_{\rm SPT}(k)$ is able to explain partially the underestimation of the valley scale. The model of $P_{\rm halofit}(k)R_{\rm sim}(k)$, which has less power at large k (Figure 6.1), can further explain

the underestimation of the valley magnitude, and give results which are closer to the simulated ones. We conclude that the suppressions of the valley scales and magnitudes observed in the simulations are due to the underestimation of $P(k)$, which originates from the lack of mode-couplings between $k < k_{\rm eff}$ and $k \geq k_{\rm eff}$.

For a simulation with box size $L_{\rm eff}$, how large is the reliable scale when studying the mean pairwise velocities? Or, if we want to study $v_{12}(r)$ to a certain scale r with simulations, how large the box size should we set? These problems can be answered from our simulations. From the upper right panel of Figure 6.3, we can read out the reliable scales $r_{\pm 10\%}$ (e.g. to 10% precision level) corresponding to simulations with different $L_{\rm eff}$. We can do the same thing for another set of our simulations ($L_{\rm box} = 1h^{-1}$Gpc), and obtain a $L_{\rm eff} - r_{\pm 10\%}$ relation, as shown in Figure 6.5. It approximates to a power law relation, and can be fitted as $L_{\rm eff} = 47.85 r_{\pm 10\%}^{0.48}$. Empirically, we can use the approximated relation of $L_{\rm eff} = 50 r_{\pm 10\%}^{1/2}$ as a guide to set up the box size of a simulation to study $v_{12}(r)$.

To correct box size effects on $v_{12}(r)$, we look at both the linear and linear+SPT correction methods. The linear corrections can be implemented as follows,

$$\begin{aligned} -\frac{v_{12,\rm LC}(r)}{Hr} &= \frac{a}{3[1+\xi_{\rm LC}(r)]}\frac{\partial \bar{\xi}_{\rm LC}(x,a)}{\partial a} \\ &= \frac{a}{3[1+\xi_{\rm sim}(r)+\Delta\xi_{\rm lin}(r)]}\frac{\partial}{\partial a}\left[\bar{\xi}_{\rm sim}(x,a)+\overline{\Delta\xi}_{\rm lin}(x,a)\right] \\ &= \frac{a}{3[1+\xi_{\rm sim}(r)]}\frac{\partial \bar{\xi}_{\rm sim}(x,a)}{\partial a}\frac{1+A_L}{1+B_L} \\ &= -\frac{v_{12,\rm sim}(r)}{Hr}\frac{1+A_L}{1+B_L}, \end{aligned} \tag{6.23}$$

or

$$v_{12,\rm LC}(r) = v_{12,\rm sim}(r)\frac{1+A_L}{1+B_L}, \tag{6.24}$$

where

$$A_L = \frac{\partial\overline{\Delta\xi}_{\rm lin}(x,a)/\partial a}{\partial\bar{\xi}_{\rm sim}(x,a)/\partial a}, \tag{6.25}$$

$$B_L = \frac{\Delta\xi_{\rm lin}(r)}{1+\xi_{\rm sim}(r)}. \tag{6.26}$$

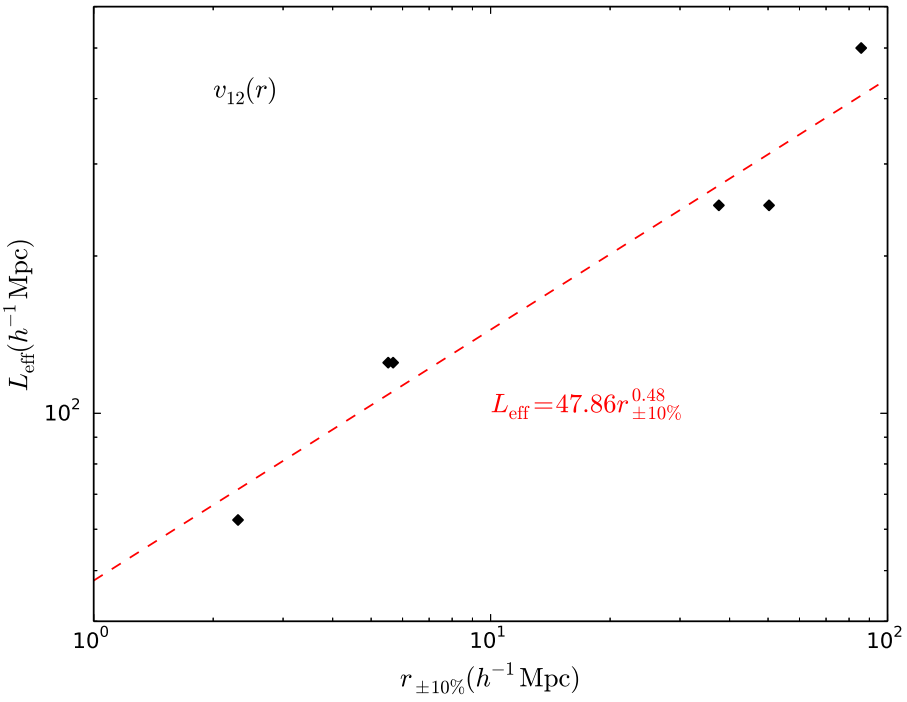

Figure 6.5: Relation between the reliable scale and the required box size for studying the mean pairwise velocities. The data from the simulations (diamonds) can be well fitted by a power law shown as the dashed line.

$\partial\bar{\xi}_{\rm sim}(x,a)/\partial a$ can be estimated as

$$\frac{\partial\bar{\xi}_{\rm sim}(x,a)}{\partial a} = -\frac{v_{12,{\rm sim}}(r)}{aHr}3\left[1+\xi_{\rm sim}(r)\right], \tag{6.27}$$

and $\partial\overline{\Delta\xi}_{\rm lin}(x,a)/\partial a$ is

$$\frac{\partial\overline{\Delta\xi}_{\rm lin}(x,a)}{\partial a} = \frac{2}{D}\frac{\partial D}{\partial a}\overline{\Delta\xi}_{\rm lin}(x,a) = \frac{2f(a)}{a}\overline{\Delta\xi}_{\rm lin}(x,a). \tag{6.28}$$

The linear corrected results are shown in the middle row of Figure 6.3. The linear corrections work well at large scales ($r > 20h^{-1}$Mpc), which confirm the results of Bagla et al. (2009). However, like the case of $\xi(r)$, at smaller scales where nonlinear clusterings start to dominate, the linear corrections gradually lose their power. An improved correction method is the linear+SPT corrections, which are summarised as

$$v_{12,{\rm LSC}}(r) = v_{12,{\rm sim}}(r)\frac{1+A_L+A_S}{1+B_L+B_S}, \tag{6.29}$$

where

$$A_S = \frac{\partial\overline{\Delta\xi}_{\rm SPT}(x,a)/\partial a}{\partial\bar{\xi}_{\rm sim}(x,a)/\partial a}, \tag{6.30}$$

$$B_S = \frac{\Delta\xi_{\rm SPT}(r)}{1+\xi_{\rm sim}(r)}. \tag{6.31}$$

Here $\partial\overline{\Delta\xi}_{\rm SPT}(x,a)/\partial a$ can be approximated as

$$\frac{\partial\overline{\Delta\xi}_{\rm SPT}(x,a)}{\partial a} = \frac{\overline{\Delta\xi}_{\rm SPT}(x,a) - \overline{\Delta\xi}_{\rm SPT}(x,a-\Delta a)}{\Delta a}, \tag{6.32}$$

where

$$\overline{\Delta\xi}_{\rm SPT}(x,a) = \frac{1}{2\pi^2}\int_{k_{\rm eff}}^{\sim k_{\rm Ny}}\Delta P_{\rm SPT}(k,a)W(kx), \tag{6.33}$$

and

$$\Delta P_{\rm SPT}(k,a) = P_{\rm sim}(k,a)\times\left[\frac{P_{{\rm SPT},L=\infty}(k,a)}{P_{{\rm SPT},L}(k,a)} - 1\right]. \tag{6.34}$$

When calculating $\Delta P_{\rm SPT}(k,a-\Delta a)$, we approximate it as

$$P_{\rm sim}(k,a-\Delta a) \approx P_{\rm SPT}(k,a-\Delta a)\times\frac{P_{\rm sim}(k,a)}{P_{\rm SPT}(k,a)}. \tag{6.35}$$

The linear+SPT corrections of $v_{12}(r)$ are shown in the lower row of Figure 6.3. Compared to the linear corrections, this correction method can further improve the corrected results in the quasi-linear regime. Especially, it works fairly well for the simulation with $L_{\rm eff} = 125\ h^{-1}$Mpc at scales $r \sim 10\ h^{-1}$Mpc.

6.4.4 Pairwise velocity dispersions

Box size effects on $\sigma_{12}(r)$ are summarised in the upper row of Figure 6.6. Simulations with small boxes tend to underestimate $\sigma_{12}(r)$ at a wide range of scales. Compared to the case of $v_{12}(r)$, the range of underestimation for $\sigma_{12}(r)$ is wider. Even at very small scales ($r \sim 0.1\ h^{-1}$Mpc), $\sigma_{12}(r)$ of the simulation with $L_{\rm eff} = 62.5\ h^{-1}$Mpc doesn't converge to the fiducial one. Also, the ratio of $\sigma_{12,L}(r)/\sigma_{12,L=500}(r)$ drops more slowly compared to the case of $v_{12}(r)$. A box size of 250 h^{-1}Mpc is enough for us to probe $\sigma_{12}(r)$ at 10% precision level up to the scale of $\sim 100\ h^{-1}$Mpc.

Due to the lack of a sophisticated model of the three-point correlation function at all scales, here we do not calculate box size effects on $\sigma_{12}(r)$ according to Equation (6.5). Instead, we consider the small r and large r limits based on CVT and CEE respectively.

At small scales ($r \lesssim 1\ h^{-1}$Mpc), we calculate $\sigma_{12}(r)$ according to Equation (6.6) for two models: (i) the halofit power spectrum chopped at $k < k_{\rm eff}$; (ii) the chopped halofit power spectrum modulated by $R_{\rm sim}(k)$. The results are shown in the left lower panel of Figure 6.6. If we assume that Q doesn't depend on $L_{\rm eff}$, or only weakly depends on it, the box size has very tiny effects on $\sigma_{12}(r)$ for model (i), which is different from the simulation results. In model (ii), by considering the modulation from $R_{\rm sim}(k)$, we observe similar box size effects as the simulations. This indicates that the underestimation of $P(k)$ [encoded by $R_{\rm sim}(k)$] is important for us to understand box size effects on $\sigma_{12}(r)$. The underestimation of $\sigma_{12}(r)$ at small scales for a simulation with small $L_{\rm eff}$ mainly originates from the lack of

mode-couplings between $k < k_{\rm eff}$ and $k \geq k_{\rm eff}$.

To calculate $\langle v_1^2 \rangle$ at large scales, we use Equation (6.9) which contains an integral of $I_2(a)$ over a. In this chapter, we only model the mode-coupling effects through $R_{\rm sim}(k)$ at $z = 0$, but we expect that these effects only become important at late time, and thus they should not affect the integral $\int_0^a da I_2(a)$ too much. Therefore, we only use the chopped halofit power spectrum to calculate $\langle v_1^2 \rangle$. The results are shown in the lower right panel of Figure 6.6. The CEE calculations give similar results as the simulated $\sigma_{12}(r)$ at large scales (e.g. $r = 100\ h^{-1}$Mpc). Especially, the CEE predictions agree better with simulations for larger $L_{\rm eff}$. We expect that the poorer agreement for the case of smaller $L_{\rm eff}$ is due to the fact that the mode-coupling effects encoded by $R_{\rm sim}(k)$ are neglected in our calculations. The ratios of $\sigma_{12,L}(r)/\sigma_{12,L=500}(r)$ predicted by CEE are marked as crosses in the upper right panel of Figure 6.6. We can use them to partially correct box size effects on $\sigma_{12}(r)$ at large scales.

In this section, we show that the couplings between the chopped and unchopped modes, which can be partially described by the one-loop SPT, are useful for understanding and correcting box size effects on the power spectra, correlation functions and pairwise velocities, especially in the quasi-linear regime. One can also consider other perturbation theories which will slightly improve the one-loop SPT results (see Carlson et al., 2009, and references therein).

6.5 Softening effects

6.5.1 Correlation functions

The effects of softening lengths on the correlation functions are shown in the upper and middle panels of Figure 6.7. The softening forces tend to flatten the correlation functions at $r \lesssim \epsilon$. For scales $r \gtrsim 2\epsilon$, the correlations functions are convergent at 10% level. Our results confirm previous studies (e.g. Jenkins et al.,

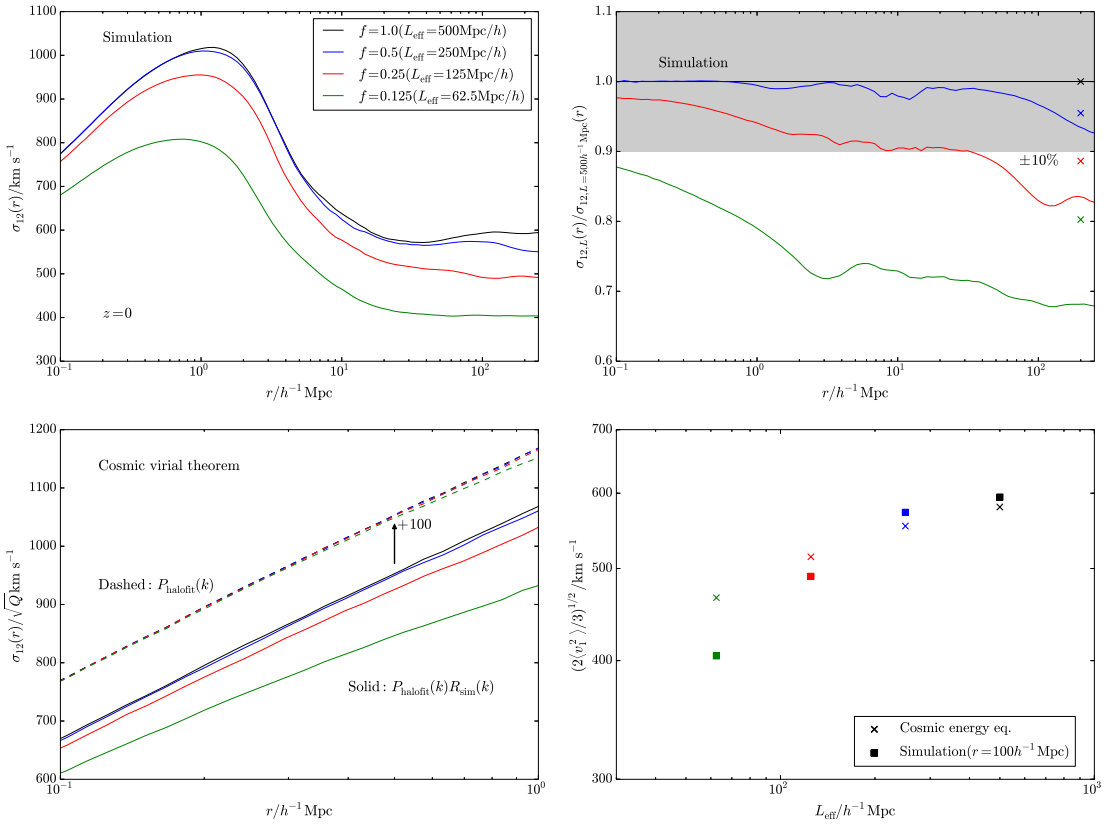

Figure 6.6: Box size effects on the pairwise velocity dispersions. The upper row summarises the results from simulations with different $L_{\rm eff}$. In the upper right panel, the shaded region shows the ±10% precision range, and the crosses mark the ratios of $\sigma_{12,L}/\sigma_{12,L=500}$ calculated from the cosmic energy equation. The lower left panel shows $\sigma_{12}(r)$ at small scales calculated from the cosmic virial theorem for two models: (i) the halofit power spectrum chopped at scales of $k < k_{\rm eff}$ (dashed); (ii) the chopped halofit power spectrum modulated by $R_{\rm sim}(k)$ (solid). To be clear, the results of model (i) are translated with 100 km s^{-1} in the $+y$-direction. The lower right panel compares $\sigma_{12}(r)$ calculated using the cosmic energy equation (crosses) with those from simulations at $r = 100\ h^{-1}$Mpc (squares). The colors mark the results with different $L_{\rm eff}$, as indicated in the legend of the upper left panel.

1998). We model the softening effects on $\xi(r)$ through the following "approximated model":

$$\xi_{\rm AM}(r) = \begin{cases} \xi_{\rm halofit}(\epsilon), r < \epsilon \\ \xi_{\rm halofit}(r), r \geq \epsilon, \end{cases} \tag{6.36}$$

where the halofit correlation function is

$$\xi_{\rm halofit}(r) = \frac{1}{2\pi^2 r} \int dk P_{\rm halofit}(k) \sin(kr) k. \tag{6.37}$$

The approximated model of $\xi_{\rm AM}(r)$ is shown in the lower panel of Figure 6.7. In the following, we will use the approximated model to understand the softening effects on the pairwise velocities.

6.5.2 Mean pairwise velocities

The upper row of Figure 6.8 presents the softening effects on the mean pairwise velocities. The softening force tends to suppress the magnitude of $v_{12}(r)$ at small scales. The mean pairwise velocities roughly converge at $r \gtrsim 4\epsilon$ at a 10% level.

Such effects can be understood qualitatively with the approximated model of the correlation functions, $\xi_{\rm AM}(r)$, as shown in the lower row of Figure 6.8. Thus, the underestimation of the magnitude of $v_{12}(r)$ at scales $r \sim \epsilon$ is due to the underestimation of the correlation functions at such scales. To explain and correct the simulated results more accurately requires a better theoretical modelling of the softening effects on $\xi(r)$, which is beyond the scope of this chapter.

6.5.3 Pairwise velocity dispersions

Softening effects on the pairwise velocity dispersions are shown in the upper row of Figure 6.9. Compared to the fiducial simulation, $\sigma_{12}(r)$ from simulations with larger ϵ are underestimated at all scales. The larger ϵ is, the larger the underestimation we observe. Especially, at large scales ($r \gtrsim 10\ h^{-1}$Mpc), the ratios of $\sigma_{12,\epsilon}(r)/\sigma_{12,\epsilon=10}(r)$ become constant (< 1).

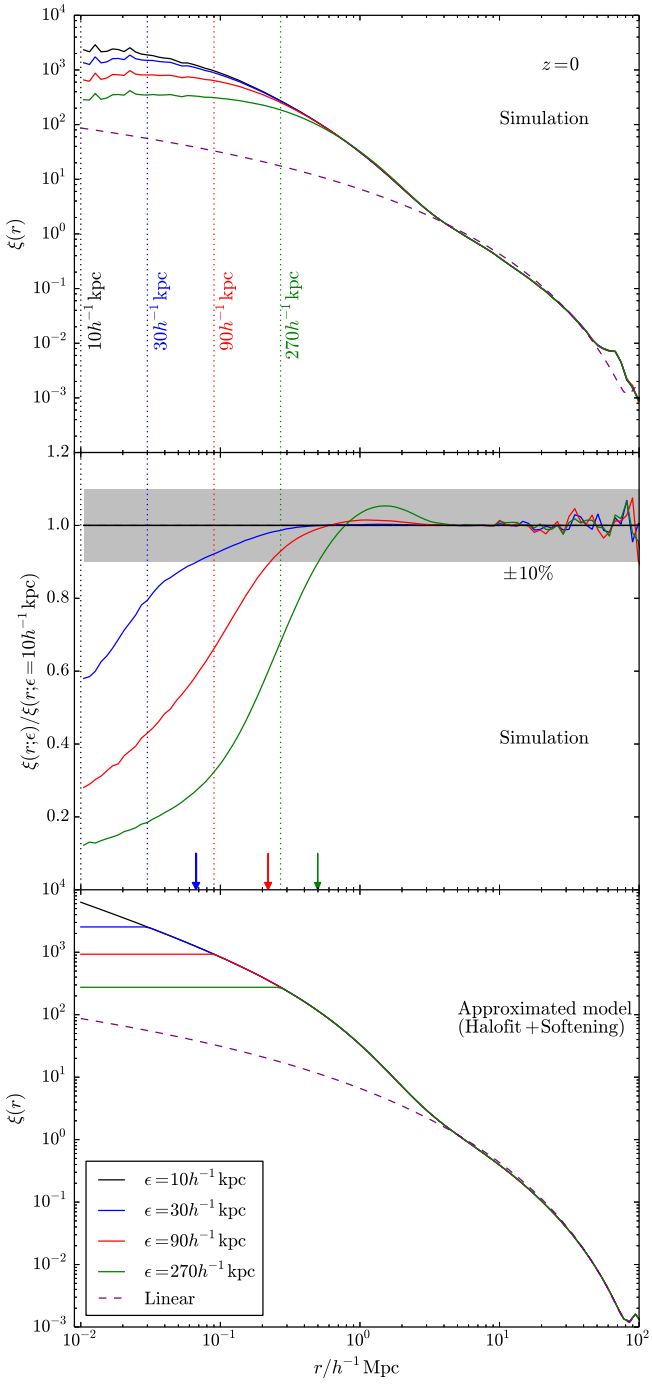

Figure 6.7: Softening effects on the correlation functions. The upper (middle) panel summarises the correlation functions $\xi(r)$ [the ratios of $\xi(r;\epsilon)/\xi(r;\epsilon=10)$] from our simulations with different softening lengths ϵ. The arrows in the middle panel mark the scale that $\xi(r;\epsilon)$ from different simulations converge to the fiducial simulation at 10% precision level. The lower panel illustrates our approximated model for the softened $\xi(r)$.

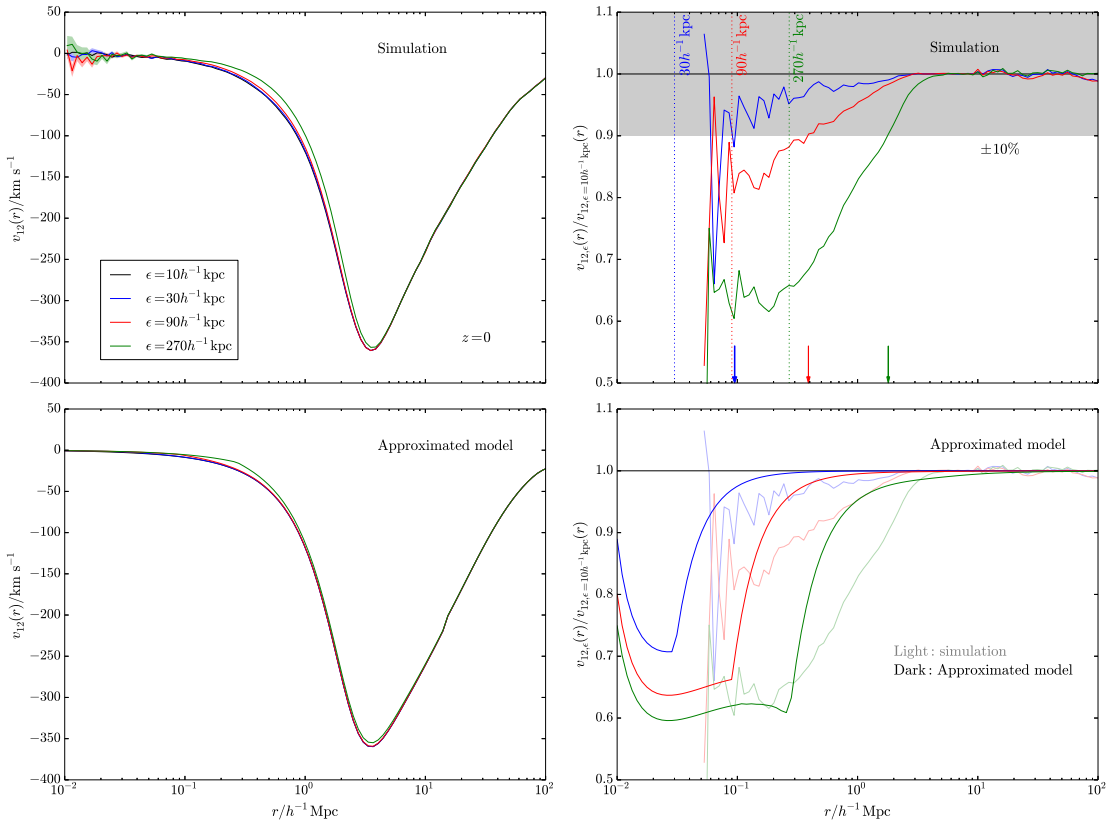

Figure 6.8: Softening effects on the mean pairwise velocities at $z = 0$. The upper row summarises $v_{12}(r)$ from the simulations with different softening lengths, as well as their ratios with respect to the fiducial simulation. The arrows in the upper right panel mark the scales of convergence at a 10% level. The ratios of $v_{12,\epsilon}(r)/v_{12,\epsilon=10}(r)$ are very noisy at $r < 0.05\ h^{-1}$Mpc, and thus are not plotted here. The lower row presents the mean pairwise velocities calculated from Equation (6.2) with $\xi_{\rm AM}(r)$. The simulated results are shown with light colors in the lower row to offer direct comparisons.

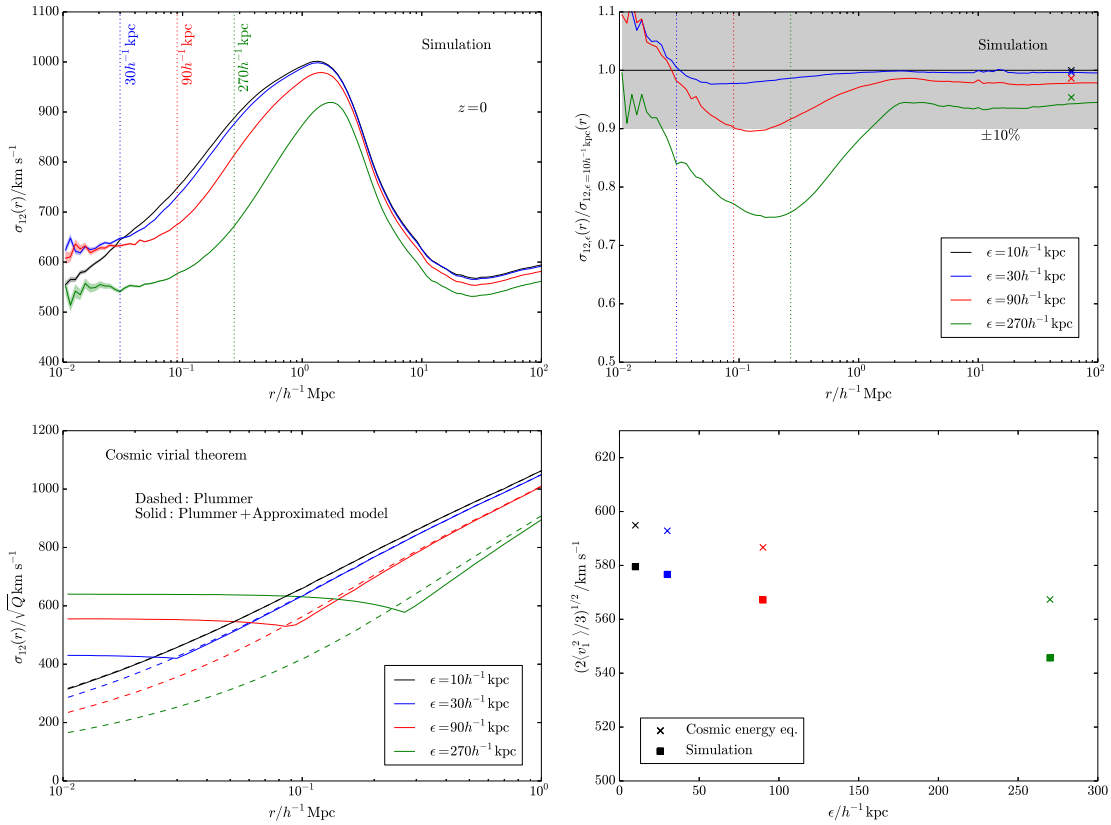

Figure 6.9: Effects of softening length on the pairwise velocity dispersions at $z = 0$. Similar to Figure 6.6, the upper row summarises the softening effects on $\sigma_{12}(r)$ from the simulations with different ϵ. The crosses in the upper right panel mark the ratios of $\sigma_{12,\epsilon}/\sigma_{12,\epsilon=10}$ calculated from the cosmic energy equation. The lower left panel shows $\sigma_{12}(r)$ at small scales calculated from the cosmic virial theorem considering: (i) Plummer's gravity only (dashed); (ii) Plummer's gravity and $\xi_{\rm AM}(x)$ of the approximated model (solid). The lower right panel compares the pairwise velocity dispersions calculated using the cosmic energy equation (crosses) with those from simulations at $r = 100\ h^{-1}$Mpc (squares).

The softening force affects $\sigma_{12}(r)$ through two approaches: (i) effectively modifying the Newtonian gravity into the Plummer softening gravity; (ii) flattening the correlation functions at small scales. As shown by the CVT calculations at small scales (lower left panel of Figure 6.9), Plummer's force leads to underestimation of $\sigma_{12}(r)$. If we further consider the effects from $\xi_{\rm AM}(r)$, we can qualitatively explain the plateaus of $\sigma_{12}(r)$ at scales $r \ll \epsilon$ observed in simulations. Of course, a quantitative estimation requires a better model of the "softened" correlation functions, as well as the three-point correlation function.

Unlike the case of $v_{12}(r)$, at large scales ($r \gg \epsilon$), $\sigma_{12}(r)$ from simulations with larger ϵ do not converge to the fiducial one. This is surprising given that we usually expect that the softening length only affects a simulation at small scales ($r \sim \epsilon$). To understand this effect, we use CEE to calculate $\langle v_1^2 \rangle$. Since we do not model the time-evolution of $\xi_{\rm AM}(r)$ here, we only consider the effects of the softened gravity on CEE. The results are shown in the lower right panel of Figure 6.9. The CEE predictions agree well with simulation results. The CEE calculations confirm that the softening force does affect $\sigma_{12}(r)$ at large scale limit. The ratios of $\sigma_{12,\epsilon}(r)/\sigma_{12,\epsilon=10}(r)$ from the CEE predictions are marked as crosses in the upper right panel of Figure 6.9, which agree fairly well with the simulated ones at large scales. This good agreement also provides a correction method for the softening effects on $\sigma_{12}(r)$ at large scales.

Actually, the softening force can induce global effects as discussed by Gerber (1996). Gerber (1996) has shown that the softening force modifies the gravitational binding energy and thus changes the equilibrium state of a galaxy. This will lead to different global properties, even at scales much larger than ϵ. The case of $\sigma_{12}(r)$ here is similar, given that the softening force modifies the potential energy and thus changes the kinetic energy through CEE, and leads to different values of the pairwise velocity dispersions at large-scale limit.

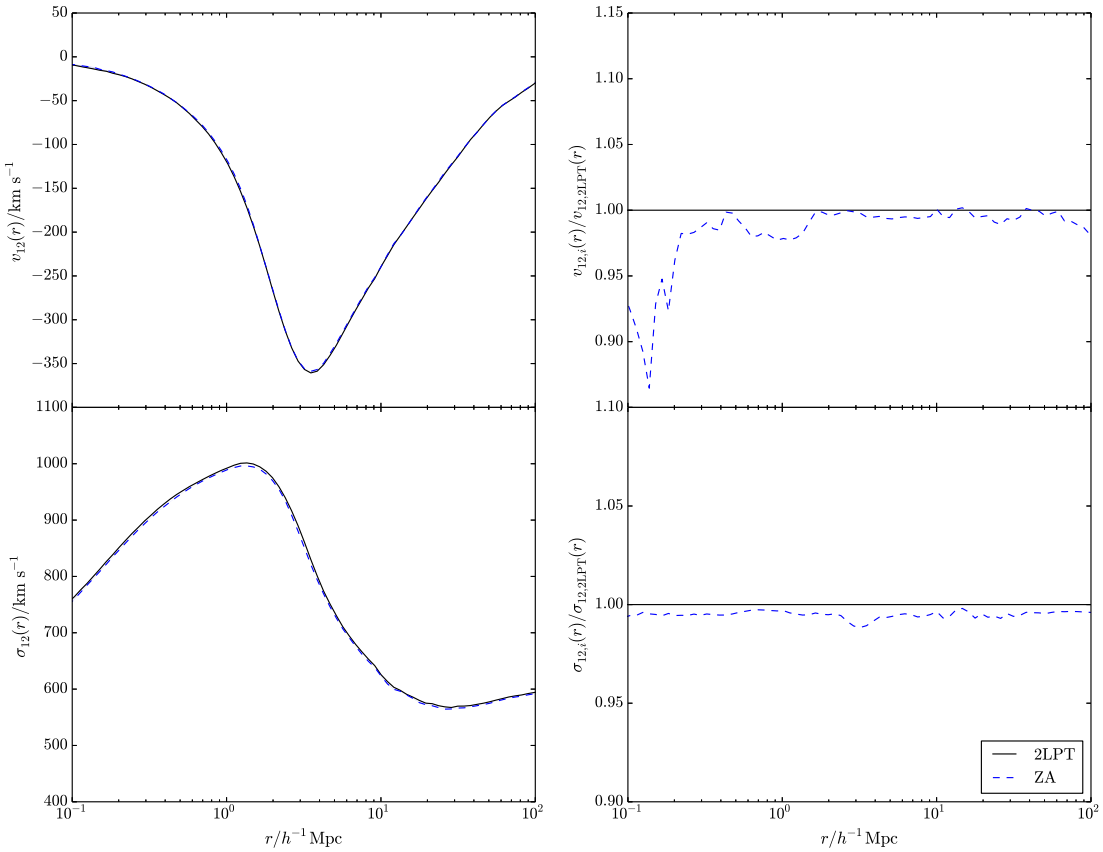

Figure 6.10: Effects of generating initial conditions with ZA (dashed) or 2LPT (solid) on the mean pairwise velocities (upper) and pairwise velocity dispersions (lower) at $z = 0$.

6.6 Effects of initial conditions

In Figure 6.10 and Figure 6.11, the effects from generating initial conditions with ZA/2LPT and grid/glass on the pairwise velocities at $z = 0$ are shown respectively. Such effects are generally very tiny; e.g. at scales $r > 0.3\ h^{-1}$Mpc, the differences between different settings are smaller than 3%. Even at smaller scales, where the effects become larger, the differences are $\lesssim 10\%$.

We conclude that the effects from initial conditions on pairwise velocities at $z = 0$ are very small and can be neglected generally.

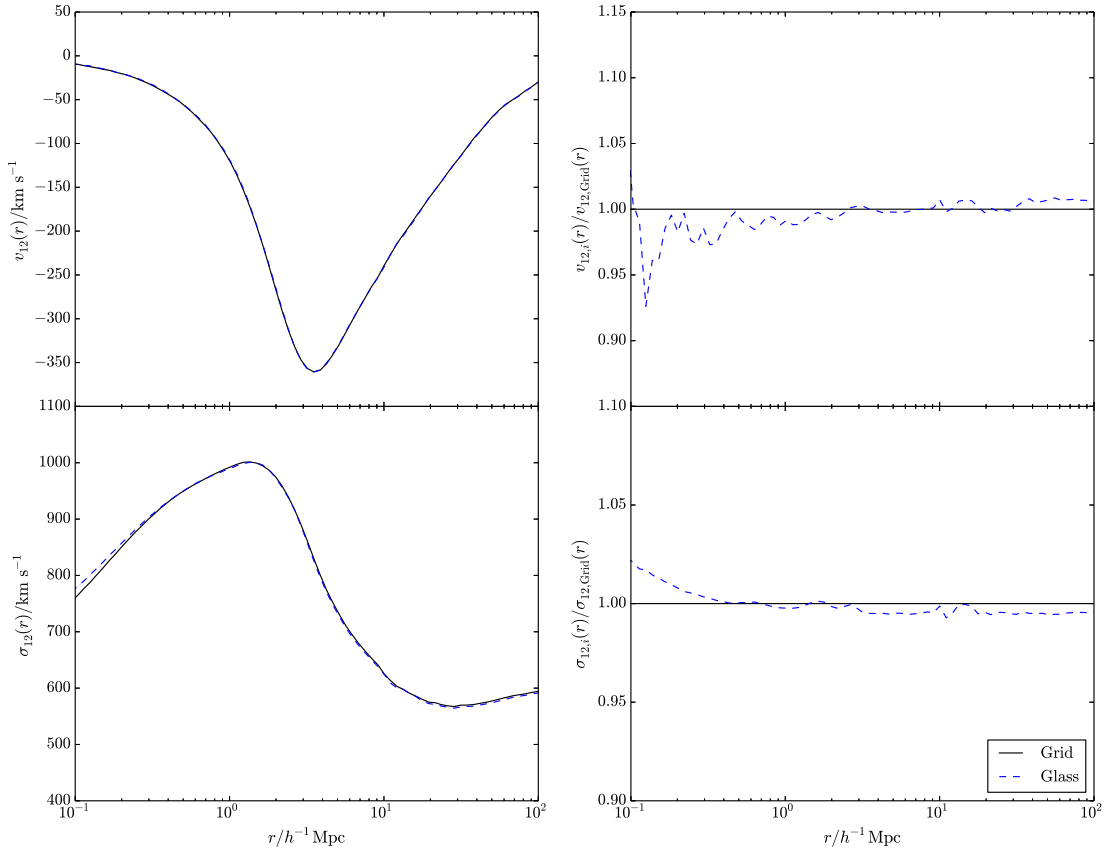

Figure 6.11: Effects of generating initial conditions with grid (solid) or glass (dashed) uniform distributions on the mean pairwise velocity (upper) and pairwise velocity dispersions (lower) at $z = 0$.

6.7 Conclusions

Given that pairwise velocities will become powerful cosmological probes in the precision era of cosmology, we need to provide very accurate theoretical predictions. The theoretical predictions of structure formation usually rely on N-body simulations, and thus the numerical effects should be carefully censored and understood. In this chapter, we perform a series of simulations to study the effects from the simulated box sizes, softening lengths and initial conditions on pairwise velocities. Our results can be summarised as follows.

(i) We confirm that the power spectra $P(k)$ and correlation functions $\xi(r)$ are suppressed at scales comparable to the simulated box size $L_{\rm eff}$ (Figures 6.1 and 6.2). We show that the couplings between modes at $k < 2\pi/L_{\rm eff}$ and $k \geq 2\pi/L_{\rm eff}$ are important to understand the suppressions, especially for simulations with $L_{\rm eff} \leq 125\ h^{-1}$Mpc. While the linear corrections significantly correct $P(k)$ and $\xi(r)$ at linear scales, the one-loop SPT, which takes the mode-couplings partially into account, can further improve corrections at quasi-linear scales. Box size effects on $P(k)$ and $\xi(r)$ are useful for understanding and correcting those on pairwise velocities.

(ii) Similar to the cases of $P(k)$ and $\xi(r)$, the mean pairwise velocities are suppressed at scales close to $L_{\rm eff}$ (Figure 6.3). Especially, for a simulation with too small a box size, the scale and magnitude of the minimum value for $v_{12}(r)$ are both underestimated. We show that such underestimations originate from the mode-coupling effects (Figure 6.4). By considering the relation between the simulated box size, $L_{\rm eff}$, and the reliable scale, $r_{\pm 10\%}$, we propose an empirical guide for the needed box size for studying $v_{12}(r)$ to a certain scale, $L_{\rm eff} = 50 r_{\pm 10\%}^{0.5}$. For example, to study the mean pairwise velocities up to 10 h^{-1}Mpc, one needs a simulation with $L_{\rm eff} \approx 150\ h^{-1}$Mpc at least.

(iii) We show that for a simulation with small $L_{\rm eff}$, the linear corrections can significantly improve the simulated $v_{12}(r)$ in the linear regime, and the one-loop

SPT can further correct $v_{12}(r)$ in the quasi-linear regime (middle and lower panels of Figure 6.3).

(iv) A simulation with a small box size ($L_{\rm eff} \leq 125\ h^{-1}$Mpc) underestimates $\sigma_{12}(r)$ in a wide range of scales, e.g. even at scales as small as $r \sim 0.1\ h^{-1}$Mpc. We show that at small scales, these underestimations can be understood with the cosmic virial theorem, and they are mainly due to the suppressions of $P(k)$. At large scales, we can use the cosmic energy equation to understand box size effects and correct them partially (Figure 6.6).

(v) The softening force leads to underestimations of the magnitude of $v_{12}(r)$ at small scales ($r \lesssim 4\epsilon$). We show in Figure 6.8 that the underestimations come from the flat correlation functions at $r < \epsilon$ which are caused by the softening (Figure 6.7).

(vi) $\sigma_{12}(r)$ can be affected by the softening force at all scales (Figure 6.9), since the softening gravity modifies the gravitational binding energy and thus changes the particle velocity dispersion $\langle v_1^2 \rangle$ through the cosmic energy equation. We show that the CEE calculations can be used to correct the softening effects at large scales quite well. At small scales, the effects from softening can be understood with the cosmic virial theorem.

(vii) We show that the effects from initial conditions (e.g. grid/glass, ZA/2LPT) on the pairwise velocities at $z = 0$ are very small and can be ignored generally.

Our results can be used as a guide for designing simulations to study pairwise velocities. For example, to study $v_{12}(r)$ at $r \in [r_{\rm min}, r_{\rm max}]$, we can set the box size and softening length according to $L_{\rm eff} = 50 r_{\rm max}^{0.5}$ and $r_{\rm min} \sim 4\epsilon$. For $\sigma_{12}(r)$, a simulation with box size $L_{\rm eff} \geq 250\ h^{-1}$Mpc is enough to probe scales up to 100 h^{-1}Mpc. Although the softening force can affect $\sigma_{12}(r)$ at large scales, the effects can be well corrected by the CEE calculations.

Our results suggest that the BBKGY hierarchy framework and one-loop SPT are very useful for understanding and correcting the numerical effects from the

finite box sizes and softening forces, which limit the range of scales that we can trust from simulations.